

Non-ideal Magnetohydrodynamic Instabilities in Protoplanetary Disks: Vertical Modes and Reflection Asymmetry

LILE WANG,^{1,2} SHENG XU,^{1,2} ZHENYU WANG,^{3,4} MIN FANG,^{5,6} AND JEREMY GOODMAN⁴

¹*The Kavli Institute for Astronomy and Astrophysics, Peking University, Beijing 100871, China*

²*Department of Astronomy, School of Physics, Peking University, Beijing 100871, China*

³*Institute of Plasma Physics, Chinese Academy of Sciences, Hefei 230031, China*

⁴*Department of Astrophysical Sciences, Princeton University, Princeton NJ 08540, USA*

⁵*Purple Mountain Observatory, Chinese Academy of Sciences, 10 Yuanhua Road, Nanjing 210023, China*

⁶*University of Science and Technology of China, Hefei 230026, China*

ABSTRACT

Magnetized disk winds and wind-driven accretion are an essential and intensively studied dispersion mechanism of protoplanetary disks. However, the stability of these mechanisms has yet to be adequately examined. This paper employs semi-analytic linear perturbation theories under non-ideal magnetohydrodynamics, focusing on disk models whose magnetic diffusivities vary by a few orders of magnitude from the disk midplane to its surface. Linear modes are distinguished by their symmetry with respect to the midplane. These modes have qualitatively different growth rates: symmetric modes almost always decay, while at least one anti-symmetric mode always has a positive growth rate. This growth rate decreases faster than the Keplerian angular velocity with cylindrical radius R in the disk and scales steeper than $R^{-5/2}$ in the fiducial disk model. The growth of anti-symmetric modes breaks the reflection symmetry across the disk equatorial plane, and may occur even in the absence of the Hall effect. In the disk regions where fully developed anti-symmetric modes occur, accretion flows appear only on one side of the disk, while disk winds occur only on the other. This may explain the asymmetry of some observed protoplanetary disk outflows.

Keywords: Magnetohydrodynamics (1964), Accretion (14), Stellar accretion disks (1579), Protoplanetary disks (1300), Exoplanet formation (492)

1. INTRODUCTION

Protoplanetary disks (PPDs), which serve as the cradles for planet formation, undergo a lifespan of approximately $10^6 - 10^7$ yr. They follow three distinct processes to disperse, namely: (1) creation of planets, (2) accretion onto the central protostar, and (3) outflowing in winds. The latter two processes directly compete with the first, impeding the time and mass available to create planets. Compared to photoevaporative winds that are mostly unable to drive accretion (Owen et al. 2012; Wang & Goodman 2017a), magnetized winds of PPD

exert torque on the disks. Magnetic fields create the linkage between disk winds and accretions and have recently been identified as a crucial factor in PPDs (Bai & Stone 2013; Bai 2013; Bai et al. 2016; Bai 2017; Wang et al. 2019). In contrast, other prospective mechanisms have inadequate efficiency in viscous turbulent accretion via the magnetorotational instability (MRI; e.g. Balbus & Hawley 1998, and the situation affected by the Ohmic resistivity, e.g. Sano & Miyama 1999) or any other hydrodynamic instabilities under PPD conditions (e.g., Bai & Stone 2013; Bai 2013; Simon et al. 2013b,a; see Turner et al. 2014 for a review).

In recent years, several studies have been conducted to investigate the magnetized wind-driven accretion process in protoplanetary disks. In one such study (Bai 2017), global simulations were performed using 2.5-dimensional axisymmetric full MHD simulations with non-ideal MHD effects. Magnetic diffusivities were eval-

Corresponding author: Lile Wang
lilew@pku.edu.cn

Corresponding author: Zhenyu Wang
zhenyu.wang@ipp.ac.cn

uated through a pre-calculated interpolation table, and thermodynamics were calculated via a simple relaxation-time recipe that accounted for temperature dependence on spatial location. Wang et al. (2019) adopted non-equilibrium thermochemical networks that co-evolved with non-ideal MHD to consistently determine all magnetic diffusivities and thermodynamic properties in real time. Building on these works, Nemer et al. (2020) performed calculations to predict observational evidence of magnetized disk winds and the resulting predictions were subsequently confirmed in recent observations. High-resolution observations of the [O I] 6300 emission line were conducted by Fang et al. (2023b), who confirmed that magnetized disk winds, rather than photoevaporative winds, were essential in explaining the spatially resolved emission line features. These studies highlight the importance of non-ideal MHD effects and the role of magnetic fields in understanding the complex dynamics of protoplanetary disks and their associated winds. There have been, nevertheless, no direct measurements of disk magnetic fields. Attempts up to now only yield the upper limits of field strengths in a handful of disks (e.g., TW Hya, Vlemmings et al. 2019; AS 209, Harrison et al. 2021).

Reflection symmetry over the equatorial plane has been commonly assumed in research on magnetized winds in protoplanetary disks, mainly concentrating on their general features, such as launching mechanisms, observables, and kinematics. Until recently, asymmetries in magnetic winds have been largely overlooked, with only a few observations indicating their existence, such as in the case of HH 30 (Watson & Stapelfeldt 2004). However, with advancements in observational techniques, more observations are expected to emerge in various wavelength bands. Understanding these asymmetries is crucial for future observations that depict detailed characteristics of magnetized disk winds. Latter et al. (2010) discovered the growth of modes with different types of reflection symmetry properties under the ideal MHD limit. Bai & Stone (2017) discussed the Hall effect and attributed the breaking of reflection symmetry to it. Béthune et al. (2017) also noticed the asymmetric accretion and wind flows in global simulations with all non-ideal MHD effects included, and attributes this effect semi-quantitatively to the expulsion of electric current sheet from the equatorial plane. Nevertheless, some recent simulation efforts discovered that the asymmetry may still emerge when the Hall effect is intentionally turned off while growth rates seem to continue. For example, Gressel et al. (2015) noticed the asymmetric pattern of accretion and wind launching in absence of the Hall effect, with Ohmic diffusivity and

ambipolar diffusion only. With local shearing box simulations, Leung & Ogilvie (2020) confirmed the growth of such anti-symmetric modes with Ohmic diffusivity only. Interestingly, Sarafidou et al. (2024) reported symmetric accretion pattern with the Hall effect involved. This paper will delve into the symmetry of wind-driven accreting protoplanetary disk systems, paying attention to their physical origins involving magnetohydrodynamics and thermochemistry and their potential observables.

This paper is structured as follows. §2 offers a detailed description of the physical models and equations used to analyze the given system. Simplified versions of the model are applied to idealized systems for qualitative discussions in §3. The mathematical models are subsequently applied to the numerical model cited in Nemer et al. (2020) to study its asymmetric instabilities, elaborated in §4. Furthermore, in §5, we explore the parameter space to understand how different physical assumptions impact the instabilities studied. Finally, §6 provides discussions on possible generalizations and observable tests and presents a summary of the principal findings and conclusions. Some details of analytic derivations are presented in the Appendices.

2. METHOD

The mathematical model of this work is based on the physical picture of wind-driven accretion in PPDs. Unless otherwise specified, this paper uses cylindrical coordinates R, φ, z for describing everything associated with the geometries, where the z -axis is aligned with the PPD's axis of rotation.

2.1. Non-ideal MHD for wind-driven accretion

This work adopts non-ideal MHD equations to describe the accretion and winds of magnetized PPDs,

$$\begin{aligned} \partial_t \rho + \nabla \cdot (\rho \mathbf{v}) &= 0, \\ \rho \partial_t \mathbf{v} + \rho \mathbf{v} \cdot \nabla \mathbf{v} &= \frac{\mathbf{J}}{c} \times \mathbf{B} - \rho \nabla \Phi - \nabla p, \\ \nabla \cdot \mathbf{B} &= 0, \quad \nabla \times \mathbf{B} = \frac{4\pi}{c} \mathbf{J}, \\ \partial_t \mathbf{B} &= -c \nabla \times \mathbf{E}, \quad \nabla \cdot \mathbf{E} = 0. \end{aligned} \quad (1)$$

Here we use ρ for the mass density, \mathbf{v} the gas velocity (c the vacuum speed of light), p the gas pressure, Φ the gravitational potential, \mathbf{J} the electric current density, and \mathbf{B} and \mathbf{E} the magnetic and electric fields. For non-ideal MHD systems with finite conductivities, the \mathbf{E} field is evaluated by the electric field in the local fluid rest frame \mathbf{E}' ,

$$\begin{aligned} \mathbf{E}' &= \mathbf{E} + \frac{\mathbf{v}}{c} \times \mathbf{B} \\ &= \frac{4\pi}{c^2} \left[\eta_O \mathbf{J} + \eta_H \frac{\mathbf{J} \times \mathbf{B}}{|\mathbf{B}|} + \eta_A \frac{\mathbf{B} \times (\mathbf{J} \times \mathbf{B})}{|\mathbf{B}|^2} \right], \end{aligned} \quad (2)$$

where $\eta_{\text{O,H,A}}$ are used to denote the Ohmic (η_{O}), Hall (η_{H}), and ambipolar (η_{A}) components of magnetic diffusivities (see also Wardle 2007; Xu & Bai 2016).

While previous studies like Wang et al. (2019) have already determined diffusivity profiles through self-consistent calculations based on non-equilibrium thermochemistry for magnetized wind-driven PPD simulations, this paper aims to explore the potential impact of hypothetical diffusivity profiles on the dynamical stability of magnetized PPDs. This approach complements previous studies and contributes to the ongoing efforts to develop more accurate and comprehensive models of the disks. Using hypothetical diffusivity profiles allows for the exploration of a range of possible scenarios and the identification of patterns or effects that may not have been previously considered, deepening our understanding of the physics of PPDs and informing future research efforts.

2.1.1. Radially local problems

In order to explore the breaking of reflection symmetry, it is necessary to have steady-state, symmetric solutions as a foundation for perturbation theories. Axisymmetric models local in cylindrical radius R are used to discuss reflection symmetry properly. In most radial ranges of typical PPDs, the vertical density scale height h is much smaller than R , which means that the derivatives of physical variables with respect to R are much smaller than those with respect to z . It is assumed that the disk gas temperature T is only a function of R . This assumption is a reasonable approximation within PPDs where T is primarily controlled by thermal accommodation with dust grains, which are in tight thermal equilibrium with the radiation emanating from the central star (Chiang & Goldreich 1997). It may not hold very well above the disk surfaces, such as inside magnetized winds (Wang et al. 2019), but our analysis focuses primarily on the behaviors below disk surfaces. For more explicit discussions, we construct isothermal models dependent only on z , with most radial derivatives ∂_R considered negligible unless otherwise specified. Because of the axisymmetry, all azimuthal derivatives (∂_φ) vanish.

To better regularize and generalize the analyses in this paper, conversions to dimensionless variables are necessary. For the radially local isothermal models we discuss,

we introduce the following conversions:

$$\begin{aligned} \zeta &\equiv \frac{z}{h}, \quad \tau \equiv \Omega_{\text{K}} t, \quad \partial_z \rightarrow \frac{\mu_k}{R} \partial_\zeta, \quad \partial_t \rightarrow \Omega_{\text{K}} \partial_\tau; \\ \mu_k &\equiv \frac{\Omega_{\text{K}} R}{c_s}, \quad \mu_\varphi \equiv \frac{v_\varphi}{c_s} - \mu_k, \quad \mu_R \equiv \frac{v_R}{c_s}, \quad \mu_z \equiv \frac{v_z}{c_s}; \\ \varrho &\equiv \frac{\rho}{\rho_0}, \quad \beta_0 \equiv \frac{8\pi c_s^2 \rho_0}{B_{z0}^2}, \quad b_i \equiv \frac{B_i}{B_{z0}}, \\ \varepsilon_i &\equiv \frac{cE_i}{c_s B_{z0}}, \quad j_i \equiv \frac{4\pi R J_i}{c B_{z0} \mu_k}, \quad i \in \{R, \varphi, z\}. \end{aligned} \quad (3)$$

Here Ω_{K} is the angular velocity of the Keplerian orbital motion, ρ_0 is the mid-plane mass density, $B_{z0} \equiv B_z|_{z=0}$ is the z -component of the magnetic fields at the equatorial plane, and the isothermal sound speed satisfies $c_s^2 = p/\rho$. The scale height is adopted as $h = c_s/\Omega_{\text{K}}$. The Mach number of Keplerian velocity μ_k compares the vertical sound crossing timescales to the orbital timescales. Its value can be estimated by,

$$\begin{aligned} \mu_k &\simeq 29 \times \left(\frac{M_*}{M_\odot}\right)^{1/2} \left(\frac{T}{300 \text{ K}}\right)^{-1/2} \\ &\quad \times \left(\frac{R}{\text{AU}}\right)^{-1/2} \left(\frac{\langle m_{\text{mol}} \rangle}{2.35 m_p}\right)^{1/2}, \end{aligned} \quad (4)$$

in which M_* is the stellar mass, m_p is the proton mass, and $\langle m_{\text{mol}} \rangle$ is the mean molecular mass. It can be easily verified that almost all radial derivatives in the dimensionless forms are multiplied by μ_k^{-1} , meaning that their effects on the equations are suppressed by more than one order of magnitude. The most important exception is $\partial_R E_z$, in which the term $\partial_R(v_\varphi B_R)$ reflects the radial velocity shear, and leads to the $(-3b_R/2)$ term in the $\partial_\tau b_\varphi$ expression without the μ_k^{-1} suppression (see also Wardle & Königl 1993). One direct consequence of this approximation is that the solenoidal condition of magnetic fields $\nabla \cdot \mathbf{B} = R^{-1} \partial_R(RB_R) + \partial_z B_z = 0$ reduces to $\partial_z B_z = 0$, and hence $b_z = 1$ always holds. Simulations of magnetized PPD winds have confirmed this assumption with high confidence (e.g. Bai 2017).

Under such transforms, the MHD differential eqs. (1) and (2) are recast into dimensionless differential equations for the axisymmetric, radial local system,

$$\begin{aligned} \partial_\tau \mu_z + \partial_\zeta \ln \varrho + \mu_z \partial_\zeta \mu_z &= \frac{2}{\beta_0 \varrho} (j_R b_\varphi - j_\varphi b_R) - \zeta, \\ \partial_\tau \mu_R + \mu_z \partial_\zeta \mu_R &= \frac{2}{\beta_0 \varrho} (j_\varphi b_z - j_z b_\varphi) + 2\mu_\varphi + g_R, \\ \partial_\tau \mu_\varphi + \mu_z \partial_\zeta \mu_\varphi &= \frac{2}{\beta_0 \varrho} (j_z b_R - j_R b_z) - \frac{\mu_R}{2}, \\ \partial_\tau b_\varphi &= -\partial_\zeta \varepsilon_R - \frac{3}{2} b_R, \quad \partial_\tau b_R = \partial_\zeta \varepsilon_\varphi. \end{aligned} \quad (5)$$

Here g_R is a correction term for reducing radial gravitational force at relatively high altitudes (see Appendix A). Note that such g_R term only directly affects

the disk accretion, not the wind launching regions or the acceleration processes within. The dimensionless electric current densities j and fluid frame electric fields ε' are related to the reduced fields b and the rest frame electric fields ε by,

$$\begin{aligned} j_R &= -\partial_\zeta b_\varphi, \quad j_\varphi = \partial_\zeta b_R, \\ \varepsilon'_R &= \varepsilon_R + (\mu_\varphi + \mu_k) b_z - \mu_z b_\varphi, \\ \varepsilon'_\varphi &= \varepsilon_\varphi + \mu_z b_R - \mu_R b_z, \quad \varepsilon'_z \simeq 0. \end{aligned} \quad (6)$$

The value of j_z is generally considered tiny, yet in some conditions, its contribution is not negligible; Appendix A also estimates the j_z values. Similar to the dimensional case, the dimensionless ε' and j are related by the magnetic diffusivities,

$$\begin{aligned} \begin{bmatrix} \varepsilon'_R \\ \varepsilon'_\varphi \end{bmatrix} &= \begin{bmatrix} \alpha_{RR} & \alpha_{R\varphi} \\ \alpha_{\varphi R} & \alpha_{\varphi\varphi} \end{bmatrix} \begin{bmatrix} j_R \\ j_\varphi \end{bmatrix}, \\ \alpha_{RR} &\equiv \alpha_O + \frac{\alpha_A}{b^2} (b_\varphi^2 + 1), \quad \alpha_{R\varphi} \equiv \frac{\alpha_H}{b} - \frac{\alpha_A}{b^2} b_R b_\varphi, \\ \alpha_{\varphi R} &\equiv -\frac{\alpha_H}{b} - \frac{\alpha_A}{b^2} b_R b_\varphi, \quad \alpha_{\varphi\varphi} \equiv \alpha_O + \frac{\alpha_A}{b^2} (b_R^2 + 1); \\ \alpha_i &\equiv \frac{\eta_i}{hc_s} \equiv \frac{2b^2}{\beta_0 \varrho} \Lambda_i^{-1}, \quad i \in \{O, H, A\}. \end{aligned} \quad (7)$$

Here $b^2 \equiv b_R^2 + b_\varphi^2 + 1$, and we also introduce $\Lambda_i \equiv B^2/(4\pi\rho\eta_i\Omega_K)$ for the Elsasser numbers of the three components. It is already known that the η_O , $\eta_H/|\mathbf{B}|$, and $\eta_A/|\mathbf{B}|^2$ are mostly independent of \mathbf{B} (e.g. Xu & Bai 2016). This fact implies that we should adopt α_O , α_H/b , and α_A/b^2 for the diffusivity profiles in practice.

2.1.2. Steady states

To solve eqs. (5) for the steady states, it is necessary to set $\partial_\tau \rightarrow 0$. Additionally, a few extra approximations can be made to simplify the problem further. In the accretion layer, vertical gas motion μ_z is significantly smaller than the horizontal motion μ_R and μ_φ . The smallness of μ_z makes the steady-state versions of eqs. (5) stiff via the operator $\mu_z \partial_z$; yet this operator is unimportant for vertically smooth solutions. Therefore, setting μ_z to zero for the system is practical. The transport of magnetic fluxes mainly affects ε_φ , which is related to radial transport, that is, $\partial_t B_z$. For a radial local solution, it is safe to assume that ε_φ is zero, allowing us to concentrate on the vertical modes. Eq. (5) are simplified by these assumptions into the ordinary differential equations (ODEs),

$$\begin{aligned} \partial_\zeta \ln \varrho &= \frac{2}{\beta_0 \varrho} (j_R b_\varphi - j_\varphi b_R) - \zeta, \quad \partial_\zeta \varepsilon_R = -\frac{3}{2} b_R, \\ \partial_\zeta b_R &= j_\varphi, \quad \partial_\zeta b_\varphi = -j_R, \end{aligned} \quad (8)$$

where the dimensionless current densities $j_{R,\varphi}$ and the subsequent velocity components are determined by solving the combination of eqs. (6) and (7) (see also Appendix B).

The symmetry required for the steady state solutions leads to $b_R = b_\varphi = 0$ at $\zeta = 0$, and $\varrho|_{\zeta=0} = 1$ by definition. The free parameter to be determined is $\varepsilon_{R0} \equiv \varepsilon_R|_{\zeta=0}$, whose value is determined by matching physical parameters of wind solutions constructed with ideal MHD. Given proper profiles of diffusivities, eqs. (8) are integrated to an altitude at which the diffusivity is sufficiently low, characterized by a critical dimensionless Ohmic diffusivity $\alpha_{O,c}$. In practice, we find that $\alpha_{O,c} = 10^{-4}$ appears to be a good cutoff, around which small variations of $\alpha_{O,c}$ will not change the results significantly. At this altitude, an ideal MHD wind solution is generated using the Bai et al. (2016) scheme, whose Bernoulli parameter should match the value given by the steady-state ‘‘disk’’ solution described here. We refer the readers to Appendix C for more details.

2.2. Linear perturbations

The stability of steady-state solutions §2.1.2 should be analyzed by perturbing eqs. (5). For any relevant dependent variables x , we decompose it into the form $x \rightarrow x + \delta x$, where the x now stands for the steady-state solution, and δx for the perturbation. This decomposition is applied to eqs. (5), (6) and (7). The perturbations of variables are preserved only up to the first order. Similar to §2.1.2, the perturbations of vertical velocities also vanish ($\delta\mu_z \rightarrow 0$) as the focus of our stability analyses is located below the disk surface.

To analyze the time evolution of the perturbations, we assume that all perturbation terms have the same time dependence, $\delta x \propto e^{\nu\tau}$, where ν is the dimensionless growth rate. The sign of ν determines whether a perturbative mode is stable ($\nu \leq 0$) or unstable ($\nu > 0$), and the absolute value of ν indicates how fast the mode grows or decays. The momentum equations for the perturbations then read,

$$\nu \delta\mu_R - 2\delta\mu_\varphi = \frac{2\delta j_\varphi}{\beta_0 \varrho}, \quad \frac{\delta\mu_R}{2} + \nu \delta\mu_\varphi = -\frac{2\delta j_R}{\beta_0 \varrho}. \quad (9)$$

The derivatives of the perturbed velocities are then,

$$\begin{aligned} \partial_\zeta \delta\mu_R &= \zeta \delta\mu_R - \left[\frac{2}{\beta_0 \varrho (1 + \nu^2)} \right] (2\partial_\zeta \delta j_R - \nu \partial_\zeta \delta j_\varphi), \\ \partial_\zeta \delta\mu_\varphi &= \zeta \delta\mu_\varphi - \left[\frac{2}{\beta_0 \varrho (1 + \nu^2)} \right] \left(\nu \partial_\zeta \delta j_R + \frac{\partial_\zeta \delta j_\varphi}{2} \right). \end{aligned} \quad (10)$$

To further simplify the analyses, we make two extra assumptions: (1) that $\delta(\ln \varrho) = 0$ (since $\mu_z \rightarrow 0$ and

$\delta\mu_z = 0$) as the linear perturbations are insufficient to reshape the vertical density profile, and (2) that the matrix elements α_{ij} ($i, j \in \{R, \varphi\}$) in eqs. (7) are not susceptible to the perturbations either. Taking the perturbations into the field equations in eqs. (5), (6) and (7), one obtains the governing equations of the perturbations, the matrix form,

$$\partial_\zeta[(A + \xi V_1)\delta b] = V_0 \delta b, \quad (11)$$

where $\delta b \equiv [\delta b_R, \delta b_\varphi, \delta j_R, \delta j_\varphi]^T$ is the vector of perturbation variables, and the other involved matrices are defined as,

$$A \equiv \begin{bmatrix} \alpha_{\varphi R} - 2\xi & \alpha_{\varphi\varphi} \\ -\alpha_{RR} & -\alpha_{R\varphi} - \xi/2 \\ -1 & \end{bmatrix}, \quad (12)$$

$$V_0 \equiv \begin{bmatrix} \nu & & & \\ 3/2 & \nu & & \\ & & 1 & \\ & & & 1 \end{bmatrix}, \quad V_1 \equiv \begin{bmatrix} & & \nu & \\ & & -\nu & \\ & 0 & & \\ 0 & & & \end{bmatrix},$$

in which $\xi \equiv 2/[\beta_0 \varrho(1 + \nu^2)]$, and we have used the approximation $\partial_\zeta \xi = \zeta \xi$ which holds inside the concerned regions (below the wind base).

Eqs. (11) are integrated with the eigenvalue ν from $\zeta = 0$ to the wind base altitude ζ_{wb} where μ_R changes the sign. Two types of symmetries are possible for $b_{R,\varphi}$:

- Symmetry: $\delta b_i = 0$ but $\partial_\zeta \delta b_i \neq 0$ at $\zeta = 0$;
- Anti-symmetry: $\delta b_i \neq 0$ but $\partial_\zeta \delta b_i = 0$ at $\zeta = 0$.

Note that, similar to §2.1, the definitions of ‘‘symmetry’’ and ‘‘anti-symmetry’’ are for the field line morphologies, viz. the integral curves of δb (see Figure 1). Because B_z should not change its sign over the equatorial plane, the symmetry in $b_{R,\varphi}$ leads to the anti-symmetry in field line morphologies and vice versa. For symmetric modes, we set the mid-plane values $\delta b_{R0} = \delta b_{\varphi 0} = 0$, $\delta j_{R0} = 1$, but $\delta j_{\varphi 0}$ as the other free parameter (the extra subscripts ‘‘0’’ here denote the $\zeta = 0$ values). For anti-symmetric modes, we fix $\delta j_{R0} = \delta j_{\varphi 0} = 0$, $\delta b_{R0} = 1$, but $\delta b_{\varphi 0}$ as the other paramter. When obtaining these type of modes, parameters ν and $\delta j_{\varphi 0}$ (symmetric) and $\delta b_{\varphi 0}$ are adjusted, so that $\delta b_R|_{\zeta=\zeta_{\text{wb}}} = \delta b_\varphi|_{\zeta=\zeta_{\text{wb}}} = 0$. This approach of setting up boundary conditions constrains the perturbations that they do not introduce shears in magnetic fields at ζ_{wb} , to avoid electric current sheets with infinitesimal thickness causing discontinuities. It also guarantees the solenoidal conditions of the perturbation fields and the radial locality of the modes. We refer the reader to Appendix D for the elaboration and analyses on these boundary conditions.

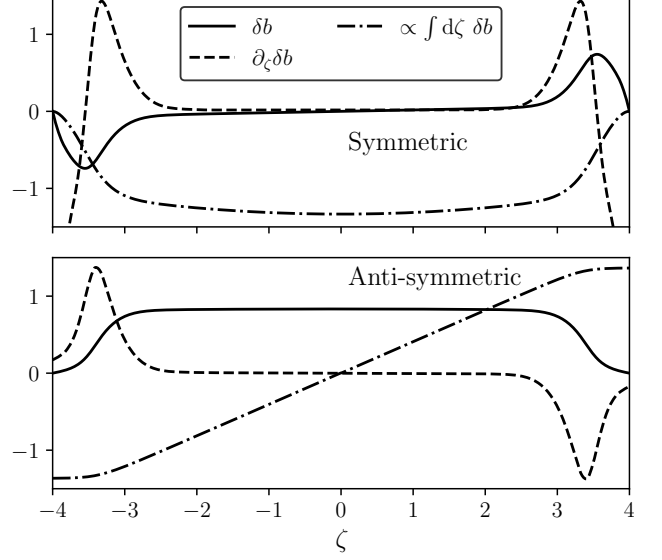


Figure 1. Schematic illustration (not to scale) of symmetric (upper panel) and anti-symmetric (lower panel) perturbation modes. Note that the symmetries are indicated in terms of field line geometries (which should refer to $\int d\zeta \delta b$), not the values of δb (§2.2).

3. STABILITIES OF SIMPLIFIED MODELS

This section applies the methods in §2 to simplified systems, which verify that our theories comply with existing studies, and also help us to acquire acquaintances with the behavior of the perturbations in PPDs.

3.1. Local ideal MHD limit

The perturbation theories derived in §2.2 quantify the finite conductivities of plasmas with non-zero dimensionless diffusivity α , and can thus be restricted to the ideal MHD limit by taking $\alpha \rightarrow 0$, yielding,

$$\begin{aligned} \partial_\tau \delta \mu_R &= \frac{2\partial_\zeta \delta b_R}{\beta_0 \varrho} + 2\delta \mu_\varphi, \quad \partial_\tau \delta \mu_\varphi = \frac{2\partial_\zeta \delta b_\varphi}{\beta_0 \varrho} - \frac{\delta \mu_R}{2}, \\ \partial_\tau \delta b_R &= \partial_\zeta \delta \mu_R, \quad \partial_\tau \delta b_\varphi = \partial_\zeta \delta \mu_\varphi - \frac{3}{2} \delta b_R. \end{aligned} \quad (13)$$

At any specific altitude, $\beta_0 \varrho$ is fixed. One usually studies the local behaviors by assuming that the coefficients can be treated as constants and Fourier transforms are applicable, i.e., $\delta x \propto e^{i(k\zeta - \omega t)}$, and the dispersion relation can be written as,

$$\begin{bmatrix} i\omega & & ik \\ -3/2 & i\omega & ik \\ 2ik/(\beta_0 \varrho) & & i\omega & 2 \\ & 2ik/(\beta_0 \varrho)k & -1/2 & i\omega \end{bmatrix} \begin{bmatrix} \delta b_R \\ \delta b_\varphi \\ \delta \mu_R \\ \delta \mu_\varphi \end{bmatrix} = 0. \quad (14)$$

This equation requires a vanishing determinant for non-trivial solutions. Defining $\tilde{k}^2 \equiv 2k^2/(\beta_0\rho)$, the dispersion relation reads,

$$\omega^4 - (2\tilde{k}^2 + 1)\omega^2 - 3\tilde{k}^2 + \tilde{k}^4 = 0. \quad (15)$$

Since ω^2 is always real, instability arises from positive imaginary parts of ω , which requires

$$\omega^2 < 0 \Rightarrow 2\tilde{k}^2 + 1 < (16\tilde{k}^2 + 1)^{1/2}, \quad (16)$$

or $\tilde{k} < \sqrt{3}$. This result is identical to the MRI dispersion relation assuming isothermal, radial local (ignoring all radial derivatives and wavenumbers) conditions (e.g. Balbus & Hawley 1991).

3.2. Constant diffusivities

A more meaningful simplification is to conduct calculations with constant, non-zero diffusivities. Similar to the ideal MHD case, we insert the perturbations into eq. (11) using the vertically local approximation and the Fourier transform scheme. Assuming that all dimensionless diffusivities ($\alpha_{O,H,A}$) are constants of ζ , the equations reduce to

$$\begin{bmatrix} i\omega & a_{\varphi R} & a_{\varphi\varphi} \\ -3/2 & i\omega & a_{RR} & a_{R\varphi} \\ & ik & 1 \\ -ik & & & 1 \end{bmatrix} \begin{bmatrix} \delta b_R \\ \delta b_\varphi \\ \delta j_R \\ \delta j_\varphi \end{bmatrix} = 0; \quad (17)$$

$$a_{\varphi R} \equiv ik\alpha_{\varphi R} - 2\xi(\zeta + ik),$$

$$a_{\varphi\varphi} \equiv ik\alpha_{\varphi\varphi} + \xi\omega(k - i\zeta),$$

$$a_{RR} \equiv -ik\alpha_{RR} - \xi\omega(k - i\zeta),$$

$$a_{R\varphi} \equiv -ik\alpha_{R\varphi} - \xi(\zeta + ik)/2.$$

Zero determinant of the matrix yields the dispersion relations. It is straightforward to verify that the dispersion relation reduces to eq. (15) once $\alpha_{O,H,A} \rightarrow 0$ and $\zeta \rightarrow 0$. An extra fact allows us to simplify the analyses further, that one shall have $\alpha_O \gg \alpha_H$ and $\alpha_O \gg \alpha_A$ inside most regions below the disk surfaces (e.g. Xu & Bai 2016), leading to,

$$\alpha_{RR} \sim \alpha_{\varphi\varphi} \sim \alpha_O, \quad \{\alpha_{RR}, \alpha_{\varphi\varphi}\} \gg \{\alpha_{\varphi R}, \alpha_{R\varphi}\}. \quad (18)$$

We use α_O and β_0 as the parameters of models. Similar to §3.1, Figure 2 plots $\nu \equiv \max\{\text{Im}[\omega]\}$ in the space spanned by the modulus of wavenumber $|k|$ and ζ for models with different α_O and β_0 . It is noted that $k \lesssim 10^0$ is unphysical in disks since the surfaces of a typical PPD is usually 2 to 3 scale heights from the equatorial plane. In addition, local calculations of the dispersion relation are only valid on spatial scales smaller than the variation lengths for typical disk parameters,

viz. $k \gg \partial_\zeta \ln \rho$. For a complete presentation, we still analytically prolongate our solutions to $|k| = 10^{-1}$, and mark the invalid regions with white shades.

In Figure 2 we observe that, at each altitude there is a critical k_{crit} that splits $\nu > 0$ and $\nu < 0$. The location of this k_{crit} is mostly insensitive to β_0 , and even insensitive to ζ , but is related to α_O . At the $\zeta \rightarrow 0$ limit, the dispersion relation reduces to

$$[\omega(1 + k^2\xi) + i\alpha_O k^2]^2 + 3k^2\xi = 0 \quad (19)$$

If one further assumes that $k^2\xi \ll 1$ (that mostly holds when $\beta_0 \gg 1$ at $\zeta = 0$) and $|\omega|^2 \ll 1$ (so that $\xi = 2/\beta_0\rho$), which follows the magnetic Reynolds number $R_m \equiv \xi(1 - \omega^2)\alpha_O^{-1} \ll 1$, such dispersion relation is identical to the weakly ionized Keplerian disk perturbations described in Sano & Miyama (1999). Such limiting case yields the highest unstable wavenumber $k_{\text{crit}} = (3\xi)^{1/2}/\alpha_O$ and the most unstable wavenumber $k_{\text{m.u.}} = k_{\text{crit}}/2$. However, considering the cases where $k^2\xi \ll 1$ or $\xi(1 - \omega^2)\alpha_O^{-1} \ll 1$ no longer holds, the actual k_{crit} could differ significantly from the previous scenarios, as one can observe by comparing the black contour (for actual k_{crit}) and the white dashed curve (for $(3\xi)^{1/2}/\alpha_O$) in Figure 2. Numerically we fit and identify that the critical k roughly follows a simple power-law, $k_{\text{crit}} \sim \alpha_O^{-1/2}$ at relatively low altitudes ($10^{-1} \lesssim \zeta \lesssim 2$).

When k_{crit} is comparable to unity, the unstable modes can grow, as the modes with vertical wavenumbers smaller than $2\pi/h$ do not exist. This criterion about the growth of instabilities agrees with the conclusions in e.g., Turner et al. (2007) and Ilgner & Nelson (2008) semi-quantitatively, although it is noteworthy that this result relies on the constant-diffusivity assumption.

4. FIDUCIAL MODEL: MAGNETIC DIFFUSIVITIES CALCULATED BY SIMULATIONS

In realistic magnetized protoplanetary disks (PPDs) models, the diffusivity profiles are vertically stratified, with a dynamical range of several orders of magnitude. In contrast to more straightforward local modes discussed in section §3, these profiles require solving eigenvalue problems (as per eq. 11) using semi-analytic methods described in section §2.2. This section's calculations rely on the non-ideal MHD profiles observed in the fiducial simulation adopted by Nemer et al. (2020) and Fang et al. (2023b).

4.1. Comparisons of steady-state solutions

In order to verify the validity of our semi-analytic approach, we compare the simulation profiles with the steady-state solutions yielded by the scheme described in §2.1.2, taking the vertical distributions of magnetic

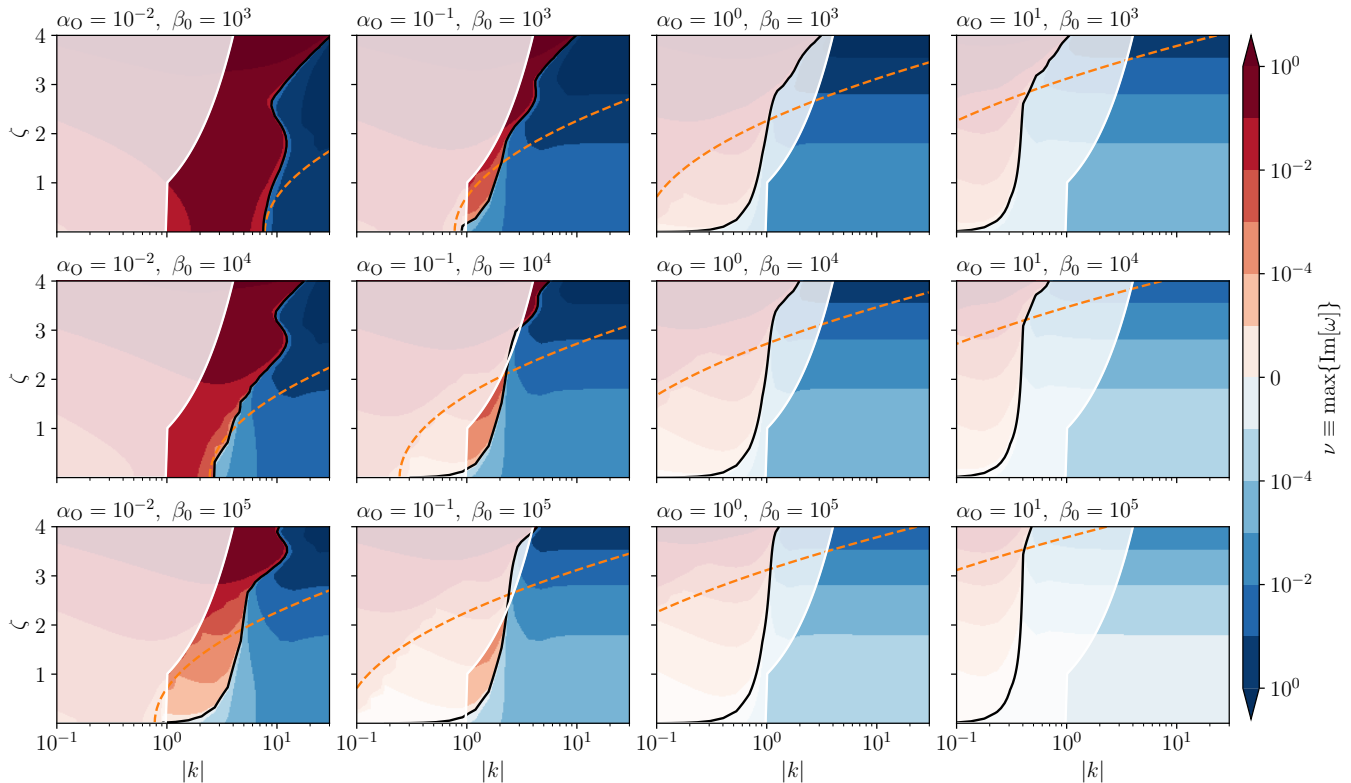


Figure 2. Local-mode growth rates ($\nu \equiv \max\{\text{Im}[\omega]\}$) assuming constant diffusivities, showing the distribution in the space spanned by the modulus of dimensionless wavenumber $|k|$ and the dimensionless altitude ζ (§3.2). The colormaps are in symmetric logarithmic scales: red for positive ν , and blue for negative ν , separated by solid black curves indicating the $\nu = 0$ contours. Dashed curves in orange indicate the limiting critical wavenumber $k = (3\xi)^{1/2}/\alpha_O$ derived in Sano & Miyama (1999) for the weakly ionized disk with magnetic Reynolds number $R_m \ll 1$. The dimensionless diffusivity α_O and the plasma β of models are presented to the upper-left of each panel. The shaded regions on the upper-left side of the white solid curves mark the regions where $k \leq \partial_\zeta \ln \varrho$ or $k \leq 1$. Local calculations of the dispersion relation are reasonable only when $k \gg \partial_\zeta \ln \varrho$ and $k > 1$, which does *not* hold within this shaded region.

diffusivities at different radii as the input. It is noticed that the $|b_R| \ll 1$ near the mid-plane, where small variations may not affect the overall behavior of the solution, yet will still change the apparent profiles in the comparisons. Here we notice that, if we define $\chi_z \equiv \partial_{\ln R} \ln B_R$, then,

$$\partial_\zeta b_R = j_\varphi + \frac{\chi_z}{\mu_k}, \quad (20)$$

and the χ_z/μ_k term will be rather important near the equatorial plane where $|j_\varphi| \simeq |\partial_\zeta b_R| \ll 1$ and $|b_R| \ll 1$. A reasonable choice is $\chi_z = -1$, which leads to $R^{-1}\partial_R(RB_R) = 0$, and $\partial_z B_z = 0$ is naturally equivalent to $\nabla \cdot \mathbf{B} = 0$. This choice also fits the $R \gtrsim 1$ AU regions in the simulations reasonably well, as it corresponds to a $B_{z0} \propto R^{-1}$ profile which largely approximates the initial magnetic fluxes at the equatorial plane. Therefore, unless specially indicated, we use $\chi_z = -1$ in what follows.

Figure 3 presents the comparisons to the simulation results at $(R/\text{AU}) \in \{0.5, 1, 2\}$, confirming that our

semi-analytic approach indeed yields consistent results. The steady-state solutions should be sufficiently regular at different radii when used as the foundation of perturbation theories. At the same time, our numerical tests have found that varying χ_z will *not* have visible impacts on the eigenvalues.

4.2. Eigenmodes of perturbations

Once the steady-state solutions have been obtained, the growth rates of perturbation modes can be calculated. For the symmetric modes, adjusting two parameters is necessary to make $\delta_{R,\varphi}$ vanish simultaneously at $\zeta = \zeta_1$, the top of the accretion layer. Because the perturbative problems are linear, one can always set $\delta j_{R0} = -[\partial_\zeta \delta b_\varphi]_{\zeta=0} = 1$, and treat $\delta j_{\varphi 0} = [\partial_\zeta \delta b_R]_{\zeta=0}$ as one of the parameters. For the anti-symmetric modes, one sets $\delta b_{R0} = 1$, and $\delta b_{\varphi 0}$ is the parameter. The other parameter in both cases is always the eigenvalue ν .

4.2.1. Eigenmodes at various disk radii

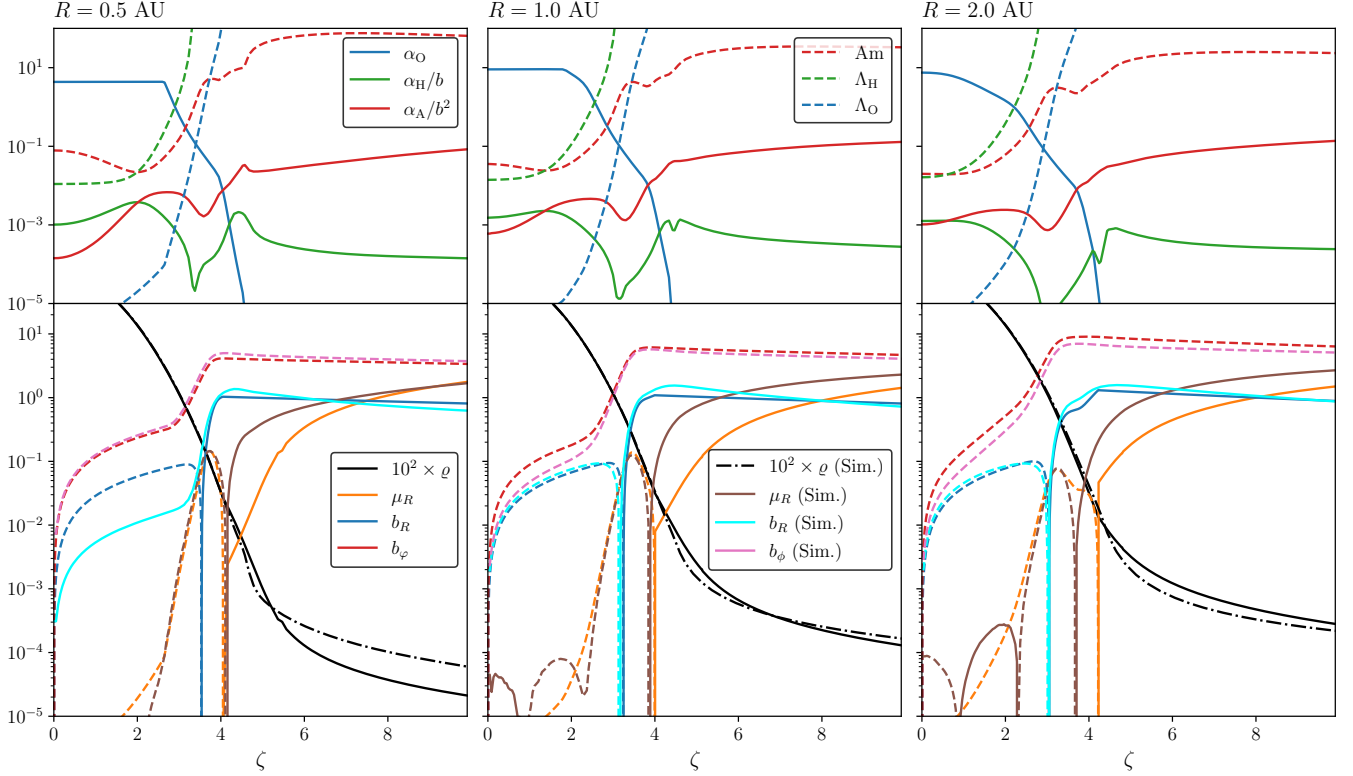


Figure 3. Non-ideal MHD profiles for the fiducial model (§4.1) at $(R/\text{AU}) \in \{0.5, 1, 2\}$ presented in different columns. **Top row:** the dimensionless diffusivities (α_O , α_H/b , and α_A/b^2) and Elsasser numbers (Λ_O , Λ_H , Am). **Bottom row** compares the key MHD profiles (ϱ , b_R , b_φ , μ_R) of the semi-analytic solutions to the simulation results [marked with “(Sim.)”] used in Nemer et al. (2020), Fang et al. (2023b). Note that in the bottom row, different physical quantities are distinguished by colors, while dashed and solid line shapes indicate negative and positive values, respectively.

We elaborate the calculations for $R/\text{AU} \in \{0.5, 1, 2\}$ as examples. Plotting the track of the zero points of $\delta b_{R1} \equiv \delta b_R|_{\zeta_1}$ and $\delta b_{\varphi 1} \equiv \delta b_\varphi|_{\zeta_1}$ in the phase space spanned by $\{\nu\} \otimes \{\delta j_{\varphi 0}/\delta j_{R0}\}$ (symmetric modes) or $\{\nu\} \otimes \{\delta b_{R0}/\delta b_{\varphi 0}\}$ (anti-symmetric modes), the proper eigen modes should locate at the intersections of the “root” curves for δb_{R1} and $\delta b_{\varphi 1}$ (Figure 4).

The first attempts to obtain eigenmodes intentionally set $\alpha_H = 0$ as the fiducial cases. For both types of modes, we observe that the modes with $|\nu| \lesssim 10^{-1}$ have the least number of nodes; modes with higher spatial frequencies all lie in the $\nu < 0$ half-space. In the $\nu > 1$ domain, the traces of roots seem to converge, but more detailed examinations confirm that they never touch each other.

At this radius, the maximum ν for symmetric modes is $\nu \simeq -0.35 < 0$ for $R = 1$ AU. Recovery of dimensions finds that this mode decays at ~ 0.4 yr per e-fold. This value is tiny compared to the disk lifetime ($\gtrsim 10^6$ yr), let alone other symmetric modes with higher spatial frequency and more negative ν . Therefore, no instability will occur through the symmetric modes. In contrast, an anti-symmetric mode with $\nu \simeq 0.0337 > 0$ exists. Am-

plitudes of this growing mode will increase by ~ 5 yr per e-fold and should leave the linear stage rather quickly.

With the current choice of magnetic diffusivity parameters, it is noteworthy that the Hall effect does not efficiently manipulate this instability. Using the $R = 1$ AU vertical Hall diffusivity profile (α_H/b) obtained based on the thermochemical profiles in Nemer et al. (2020), we test the situations that B_z is parallel and anti-parallel to the axis of disk rotation, respectively. The resulting eigenvalues are affected by a tiny fraction ($\nu = 0.0343$ for parallel fields and $\nu = 0.0332$ for anti-parallel fields). This consequence seems to be in odd to some previous studies concluding that the Hall effect could lead to significant asymmetries across the equatorial plane (e.g. Lesur et al. 2014; Bai & Stone 2017). We point out that the apparent discrepancy originates from the distinct magnetic diffusivity profiles selected for the disk model. The profiles utilized in the work of Nemer et al. (2020) result in a ratio of $|\alpha_H/b|/\alpha_O$ that is less than 10^{-1} (and frequently even $\lesssim 10^{-3}$) beneath the disk surfaces (see also Figure 3). It is essential to recognize that the actual magnetic diffusivity profiles are contingent upon the thermochemical conditions at hand, which re-

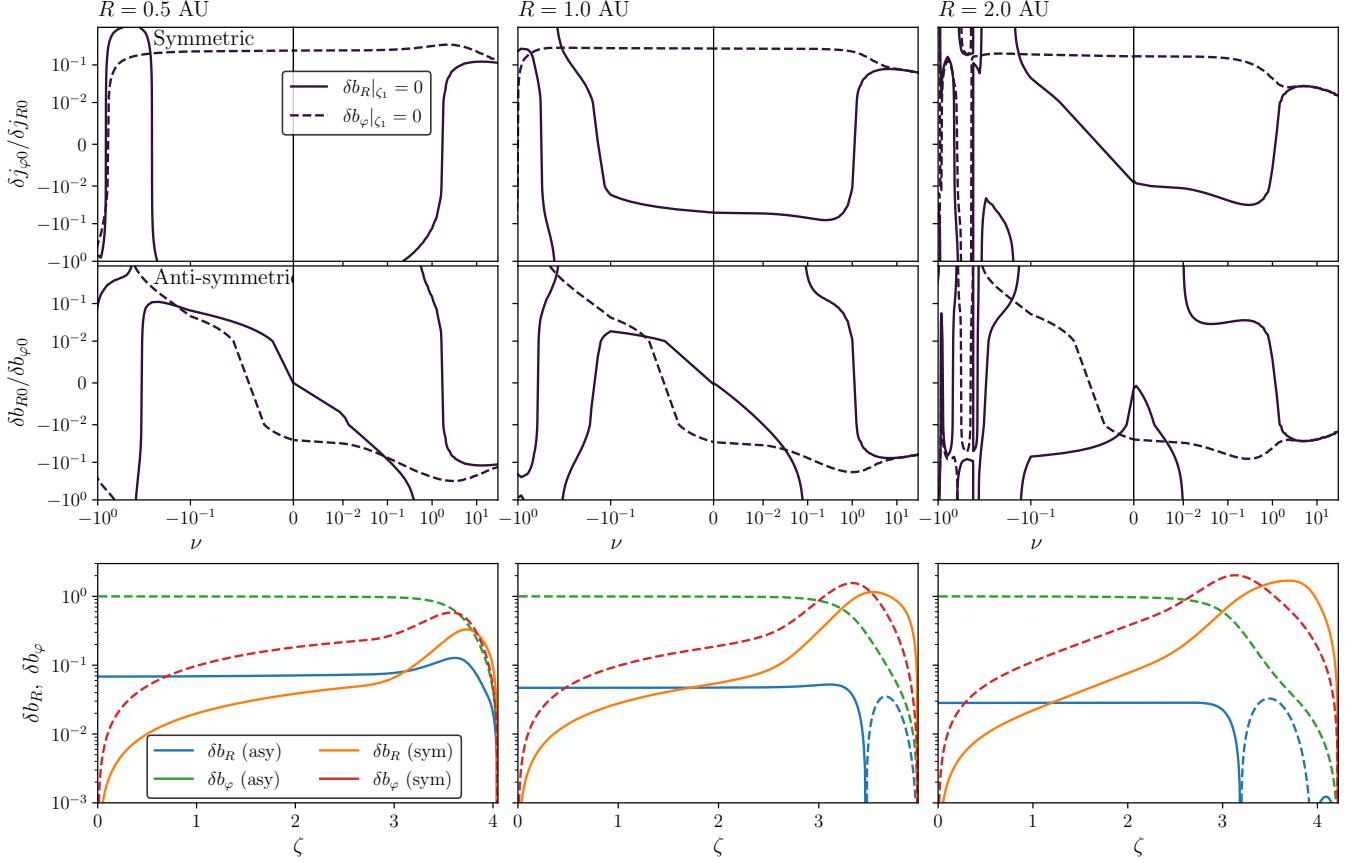


Figure 4. Eigensolutions at disk radii (R/AU) $\in \{0.5, 1, 2\}$ presented in different columns (see also §4.2.1). The **top row** shows the phase diagrams for the symmetric perturbation modes in the space spanned by the dimensionless $\{\nu_{\text{sym}}\} \times \{\delta j_{\varphi 0} / \delta j_{R0}\}$. The solid and dashed contours indicate the tracks of $\delta b_R|_{\zeta_1} = 0$ and $\delta b_{\varphi}|_{\zeta_1} = 0$ (ζ_1 is the altitude of the wind base), respectively, and their intersections indicate eigensolutions. Note that the negative- ν and positive- ν regions, separated by a vertical solid line, have different scales in ν . The **middle row** is similar to the top row but shows the phase diagrams for the anti-symmetric modes in the $\{\nu_{\text{asy}}\} \times \{\delta b_{R0} / \delta b_{\varphi 0}\}$ phase space. The **bottom row** presents the eigensolutions with the largest growth rates for both modes. Note that the symmetric modes always have negative growth rates, and that the tracks seem to converge at large positive ν but they never cross each other indeed.

sult from the specific thermochemical network employed and the astrophysical conditions of the concerned regions, such as the high-energy radiation luminosity emitted by the central star. The Hall diffusivity profiles that have been integrated into studies concentrating on the Hall shear instability and subsequent symmetry breaking (e.g. Lesur et al. 2014; Bai & Stone 2017; Sarafidou et al. 2024) are typically significantly higher. Once $|\alpha_{\text{H}}/b| \gtrsim \alpha_{\text{O}}$, local analyses similar to §3.2 reveals that the modes become significantly more unstable: the critical wavenumber of instability becomes $\gtrsim 10\times$ greater than the current values. In the meantime, even the results assuming $\alpha_{\text{H}}/b \ll \alpha_{\text{O}}$ do *not* deny the importance of the Hall effect. The nature of the spontaneous symmetry breaking can the Hall effect could be the “first push” that determines the direction, and the subsequent

amplification of asymmetry is dominated by the instabilities described in this section.

4.2.2. Scalings of eigenvalues

When the scheme described in §4.2.1 is applied to all relevant radii in the disk model in §4.1, stability conditions of the disk can be studied in terms of the reflection symmetry. After multiplied by the local Keplerian angular velocity to recover the dimensions, we present the dimensional growth rates as functions of disk radius in Figure 5— $\tilde{\nu}_{\text{sym}}$ for the symmetric mode, and $\tilde{\nu}_{\text{asy}}$ for the anti-symmetric mode. It is evident that throughout all radii in the model $\tilde{\nu}_{\text{sym}} < 0$ but $\tilde{\nu}_{\text{asy}} > 0$, thus symmetric modes always decay, but at least one of the anti-symmetric modes grows. In other words, the reflective symmetric morphology of the wind-driven accretion

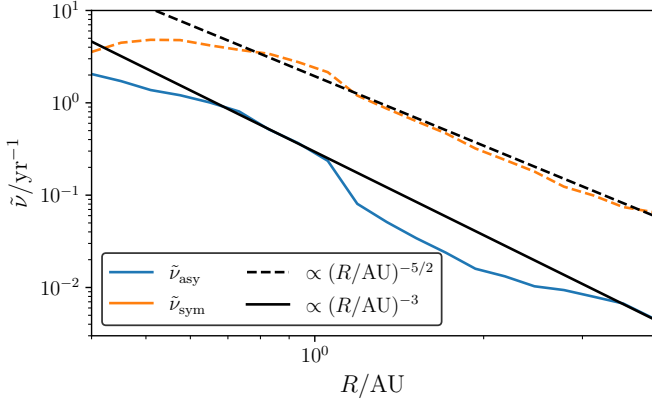


Figure 5. Dimensional growth rates of anti-symmetric ($\tilde{\nu}_{\text{asy}}$) and symmetric ($\tilde{\nu}_{\text{sym}}$) modes (dashed line for negative values), for the fiducial model through the range of disk radius $0.4 < (R/\text{AU}) < 4$. Note that $\tilde{\nu}_{\text{sym}} < 0$ holds for all radii. The lines indicating the $R^{-5/2}$ and R^{-3} power-laws are also presented for comparison.

model is unstable, and the instability always initiates in an anti-symmetric shape.

For both $\tilde{\nu}_{\text{asy}}$ and the $|\tilde{\nu}_{\text{sym}}|$ at $R \gtrsim 0.6$ AU, one can roughly read their scaling from Figure 5,

$$\frac{|\tilde{\nu}_{\text{sym}}|}{\text{yr}^{-1}} \sim 2 \times \left(\frac{R}{\text{AU}}\right)^{-5/2}, \quad \frac{\tilde{\nu}_{\text{asy}}}{\text{yr}^{-1}} \sim 0.2 \times \left(\frac{R}{\text{AU}}\right)^{-3}. \quad (21)$$

The growth and decay rates decrease with radius faster than Ω_K . For larger radii, the growth of anti-symmetric modes could be slow. If the scaling relation in eq. (21) can be generalized to all concerned radii in a typical PPD, then $\tilde{\nu}_{\text{asy}}^{-1}$ could be as slow as $\sim 2.5 \times 10^6$ yr at $R \sim 200$ AU, presumably the “typical” outer radius of PPDs: the anti-symmetric instability will marginally grow through the $\sim 10^6 - 10^7$ yr lifetime of a PPD. The growth is challenging to identify in numerical simulations available at such a large distance, and hence, the necessity of the analytic approach is emphasized.

4.3. Evolution of the anti-symmetric modes

For the breaking of reflection symmetry, we have identified that a possible evolution manner is a quasi-steady state, whose most prominent characteristic is the asymmetric wind-driven accretion flow. To construct the morphologies analytically, we slightly modify the methods in §2.1.2 by setting non-vanishing b_R and b_φ at the mid-plane and integrating to both $+\zeta$ and $-\zeta$ directions. When obtaining such models, the matching onto ideal MHD wind solutions is carried out only on the wind-launching side, and the other side is left free. This scheme will leave the mid-plane b_{R0} and $b_{\varphi0}$ unconstrained. These two degrees of freedom reserve the

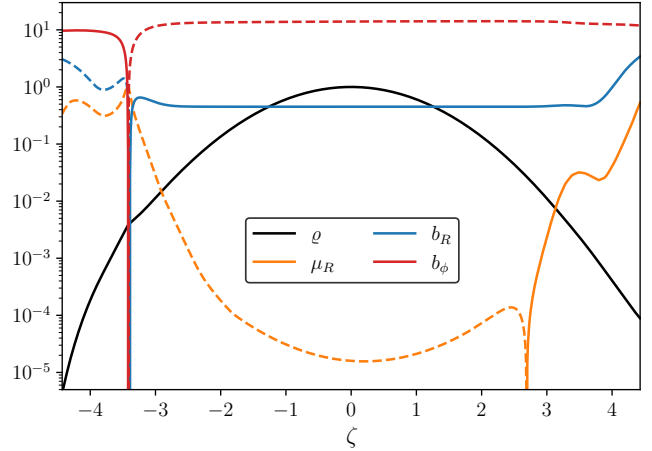


Figure 6. Similar to the lower row of Figure 3 but showing a non-symmetric solution using the diffusivity profiles at $R = 1$ AU as an example. Colors distinguish different physical quantities, while the line shapes indicate the signs (solid for positive, dashed for negative).

tracks of growth for the anti-symmetric modes, allowing a selection of $(b_{R0}, b_{\varphi0})$ reflects a snapshot in the path of growth before saturation. In general, the evolution of instabilities could be a complicated issue that requires excessive numerical experiments to understand, and we leave these studies to future works.

Figure 6 illustrates the MHD profiles obtained at $R = 1$ AU, in which we set $b_\varphi|_{\zeta=0} = -14$, and the mid-plane value of b_R is fixed at $b_R|_{\zeta=0} = 0.45$. In this model, the accretion mainly occurs on the $\zeta < 0$ side, while the disk wind is launched efficiently only on the $\zeta > 0$ side. Over the disk surface on the $\zeta < 0$ side, suppression of gas density is observed, and μ_R is always negative. Such a combination of fluid parameters indicates an absence of wind over that surface.

The one-sided wind launching feature implies that the disk wind will exhibit an apparent “asymmetric” shape. Such phenomenon has been observed in various non-ideal MHD simulations of PPDs, in which the asymmetries developed to different extents (e.g. Bai 2017; Hu et al. 2019; Riols et al. 2020; Hu et al. 2022; X. Hu et al., in prep.). Calculations in this work have confirmed that these asymmetric morphologies should be physically plausible, and we should also expect to discover such asymmetries observationally (see discussions in §6.2).

5. STABILITY IN VARIOUS MHD MODELS

The wind-driven accretion problem described in §6.2:fid-model is a typical PPD model, yet countless situations still need to be discussed. The diversity of PPDs, including their mass distributions, host star properties,

and thermochemical conditions, can all affect the diffusivity profiles significantly. To study those parameters, this section explores different disk conditions, including gravitation, magnetization, and diffusivity profiles. We will manipulate one parameter at a time to simplify and clarify the elaborations.

5.1. Functional forms of the vertical diffusivity profiles

For typical PPDs, the vertical stratification of diffusivities can be qualitatively divided into three regions, (1) the weak coupling mid-plane ($\alpha_{\text{O}} \sim 10^1$) in the $\zeta \lesssim 2$ region, (2) the transition layer near the disk surface ($10^1 \gtrsim \alpha_{\text{O}} \gtrsim 10^{-4}$, $2 \lesssim \zeta/h \lesssim 4$), and (3) the highly ionized wind above. As we have verified that the Hall effect is more critical as a “first-push” than an amplification mechanism, the following discussions will focus on the Ohmic and ambipolar diffusivities. We choose to parameterize α_{O} and α_{A}/b^2 , as they are insensitive to magnetic field strengths. Simple log-linear functions with caps parameterize the vertical profiles of diffusivities ($\zeta' \equiv \max\{\zeta - \zeta_t, 0\}$),

$$\begin{aligned} \log_{10} \alpha_{\text{O}} &= \log_{10} \alpha_{\text{O}0} + \psi_{\text{O}} \zeta', \\ \log_{10}(\alpha_{\text{A}}/b^2) &= \log_{10}(\alpha_{\text{A}}/b^2)_0 + \psi_{\text{A}} \zeta', \end{aligned} \quad (22)$$

where $\alpha_{\text{O}0}$ and $(\alpha_{\text{A}}/b^2)_0$ are the values at the equatorial plane, ψ_{O} and ψ_{A} are the slopes in the logarithmic space, and ζ_t marks the transition altitude. In §4 we already found that ϱ profiles are almost unaffected by the accretion and remain almost identical to the static disk. In addition, although the radial derivative of B_z may affect the b_R near the mid-plane in steady-state solutions, we have nevertheless confirmed that this hardly affects the growth rates of perturbation modes. Therefore, we take the approximations that $\rho = \exp(-\zeta^2/2)$ and $\chi_z = 0$ (§4.1) for all models in this section to make the results independent of R .

A reference model is constructed and illustrated in the left column of Figure 7. This model has $\alpha_{\text{O}0} = 10^1$, $(\alpha_{\text{A}}/b^2)_0 = 10^{-3}$, $\psi_{\text{O}} = -2$, $\psi_{\text{A}} = 0.5$, and $\zeta_t = 2.5$, which qualitatively resembles the $R = 1$ AU slice of the fiducial model in §4.1. The consequent steady-state solution is also quite similar. For the perturbation modes, the symmetric mode has decay rate $\nu_{\text{sym}} \simeq -0.42$, which has the same sign, but the absolute value is different by $\sim 20\%$. The growth rate of the anti-symmetric mode is $\nu_{\text{asy}} = 0.061$, $\sim 50\%$ different from the results based on the simulation diffusivity profiles.

5.2. Impacts of MHD parameters

The reference model described in §5.1 is modified to study the influence of different parameters. We first confirm that μ_k , which reflects the relative importance

of orbital motion, only plays a secondary role: taking $\mu_k \in [4, 10^2]$ only leads to minor variations in ν , such that $-0.063 \gtrsim \nu_{\text{sym}} \gtrsim -0.10$ and $0.03 \lesssim \nu_{\text{asy}} \lesssim 0.04$. In contrast, the magnetization parameterized by β_0 is a significant parameter. As shown in Figure 7, the stronger the disk’s magnetization (or smaller β_0), the faster the perturbation modes grow or decay. If one sets $\beta_0 = 10^3$ based on the reference model, such a strong magnetization yields $\nu_{\text{sym}} \simeq -1.0$ and $\nu_{\text{asy}} \simeq 0.38$, leading to an e-fold increase of anti-symmetric amplitude every half orbit period. With $\beta_0 \lesssim 10^5$, the growth or decay rates scale roughly as $\sim \beta_0^{-1/2}$, or roughly linearly with field strength.

Different components of magnetic diffusivities control the stability problem in different ways. The ambipolar diffusion parameter $(\alpha_{\text{A}}/b^2)_0$ affects both ν_{sym} and ν_{asy} , yet the absolute values of both ν vary rather reluctantly as the parameter stay in the range $(\alpha_{\text{A}}/b^2)_0 \in [10^{-4}, 10^{-2}]$. The situation is similar about the dependence of ν_{asy} upon $\alpha_{\text{O}0}$ and ζ_t . When we examine the symmetric modes, however, it is found that ν_{sym} becomes positive when $\alpha_{\text{O}0} \lesssim 0.6$, or $\zeta_t \lesssim 1.4$. As the conductivity in the adjacency of the mid-plane becomes higher, by either lowering the $\alpha_{\text{O}0}$ or setting a lower transition altitude ζ_t , the stronger coupling between field and fluids eventually leads to the instability even for the symmetric modes. The threshold value for $\alpha_{\text{O}0}$ also matches the vertically local mode calculations in §3.2 semi-quantitatively. Meanwhile, ν_{asy} does not change sign throughout the subset of parameter space we explored and illustrated in Figure 7, neither in the search over a broader span of the parameter space that is not elaborated here. This fact indicates the ubiquity of the instability for the anti-symmetric modes.

6. DISCUSSIONS AND SUMMARY

This study explores the instability that leads to reflection symmetry breaking over the equatorial planes in protoplanetary disks (PPDs) that go through wind-driven accretion. We develop linear perturbation theories using steady-state solutions and evaluate eigenmodes and their corresponding eigenvalues with different symmetries. Symmetric perturbations always decay under typical MHD profiles, whereas at least one of the anti-symmetric modes has a positive growth rate. The growth of anti-symmetric modes leads to tilted disk kinematics, where the accretion flow occurs on one side, and the disk wind is launched on the other. We also investigate the effects of varying magnetic diffusivity profiles on the reflection symmetry breaking, finding that the anti-symmetry is most prominent in regions of the disk with poorly ionized mid-plane where fields and fluids are

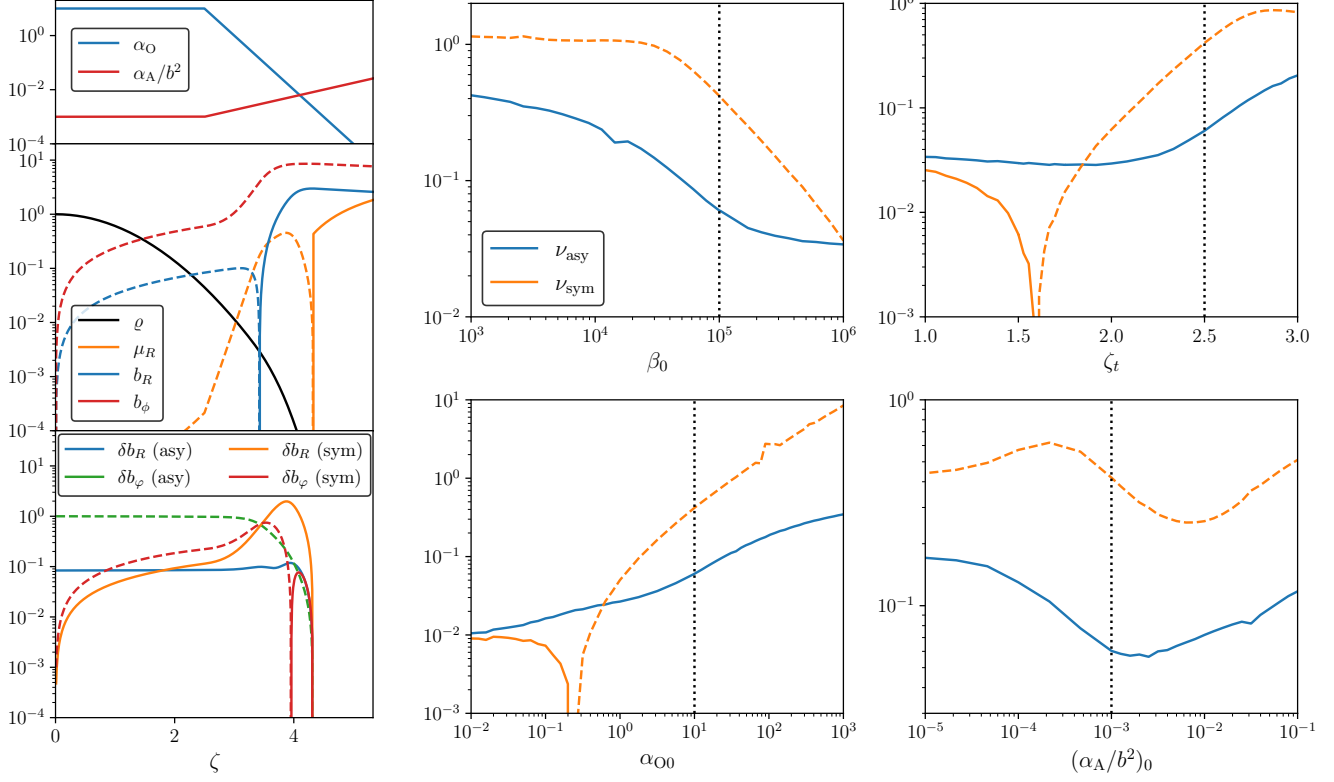


Figure 7. Left column illustrate the model for reference with the setup in §5.1, showing the diffusivity profiles (upper panel), the steady-state solution (middle panel), and the perturbation modes (lower panel). The growth rates are $\nu_{sym} = -0.10$ and $\nu_{asy} = 0.035$. Right two columns present the dependence of ν_{sym} (orange lines) and ν_{asy} (blue lines) on different parameters: β_0 , ζ_t , α_{00} , and $(\alpha_A/b^2)_0$ (see §5.2). Note that negative values are shown in dashed lines. The vertical dotted lines are plotted in each panel indicating the value taken by the reference model.

weakly coupled and intermediate surface layers where the ionization and field-fluid coupling are intermediate.

6.1. Qualitative behavior of eigenvalues

Qualitative discussions on the behaviors of eigenvalues are necessary to develop physical insights into the findings of this paper and guide future explorations. Eq. (12) can be recast in the integrated form,

$$[(A + \xi V_1)\delta b]_{\zeta_0}^{\zeta_1} = V_0 \int_{\zeta_0}^{\zeta_1} \delta b \, d\zeta. \quad (23)$$

Since we are most interested in the modes with the least nodes, especially the prospectively anti-symmetric modes with anti-symmetry, the approximation $\nu \ll 1$ can be safely adopted, hence $\xi \simeq 2/(\beta_0 \varrho)$. The bottom two rows in the matrix form of eq. (23) are indeed equivalent to $\delta j_R = -\partial_\zeta \delta b_\varphi$ and $\delta j_\varphi = \partial_\zeta \delta b_R$, while the top

two rows should be analysed for ν ,

$$\begin{aligned} \nu \mathcal{B}_R &= [\alpha_{\varphi\varphi} \delta j_\varphi + (\alpha_{\varphi R} - 2\xi) \delta j_R]_{\zeta_0}^{\zeta_1}, \\ \nu \mathcal{B}_\varphi &= [\alpha_{RR} \delta j_R + (\alpha_{R\varphi} - \xi/2) \delta j_\varphi]_{\zeta_0}^{\zeta_1} + \frac{3}{2} \int_{\zeta_0}^{\zeta_1} \delta b_R \, d\zeta; \\ \mathcal{B}_R &\equiv \int_{\zeta_0}^{\zeta_1} \delta b_R \, d\zeta - (\xi \delta j_\varphi)_{\zeta_0}^{\zeta_1}, \\ \mathcal{B}_\varphi &\equiv - \int_{\zeta_0}^{\zeta_1} \delta b_R \, d\zeta - (\xi \delta j_R)_{\zeta_0}^{\zeta_1}. \end{aligned} \quad (24)$$

6.1.1. Anti-symmetric modes

For the anti-symmetric modes, the equation for $\delta \tilde{b}_R$ is typically easier to analyze by locating $\zeta_0 = 0$ (at which $\delta j_R = \delta j_\varphi = 0$) and ζ_1 at the first zero point of δb_R (likely the wind base). Without loss of generality, the linearity of the equations allows one to set $\delta b_R > 0$ throughout all altitudes in the concerned modes, which in turn yields $\delta b_\varphi < 0$, $\delta j_R|_{\zeta_1} = -[\partial_\zeta \delta b_\varphi]_{\zeta_1} < 0$, and $\delta j_\varphi|_{\zeta_1} < 0$ due to the geometries of disks and fields. The coefficient \mathcal{B}_R on is therefore positive definite, and the sign of ν depends on the right-hand side.

The cases that we concern usually have $|\delta b_\varphi|_{\zeta_1} \gg |b_R|_{\zeta_1}$ due to the amplification of toroidal fields by rotation, expecting that $|\delta j_R|_{\zeta_1} \gg |\delta j_\varphi|_{\zeta_1}$. In the meantime, the wind base usually have $\alpha_A/b^2 \sim \alpha_O$, therefore $|b_\varphi|_{\zeta_1} \gg |b_R|_{\zeta_1}$ usually leads to $|\alpha_{\varphi R}|_{\zeta_1} \gg |\alpha_{\varphi\varphi}|_{\zeta_1}$, which have been confirmed by all cases involved in §4. These facts focus on the competition between $\alpha_{\varphi R}$ and 2ξ at ζ_1 . Since b_R and b_φ have different signs at the wind base due to the disk geometries and MHD configurations, $\alpha_{\varphi R}|_{\zeta_1} > 0$ always holds. Our numerical experiments have found $\alpha_{\varphi R}|_{\zeta_1} < 2\xi|_{\zeta_1}$ throughout the fiducial model, which is consistent with the finding that $\nu > 0$, i.e. there are always unstable anti-symmetric modes (Figure 5). In order to eliminate the instability, the inequality $\alpha_{\varphi R}|_{\zeta_1} < 2\xi|_{\zeta_1}$ has to be reverted.

6.1.2. Symmetric modes

The symmetric modes are easier to analyze by still setting $\zeta_0 = 0$ but locate ζ_1 at the first zero point of $\delta j_R = -\partial_\zeta \delta b_\varphi$. With such selection, it is easy to verify that $\delta j_{R,\varphi}|_{\zeta_0} > 0$. Also, taking $\delta b_R > 0$ at $\zeta > 0$ due to linearity, one can prove that \mathcal{B}_R is still positive. On the right-hand side, $[\alpha_{\varphi\varphi} j_\varphi]_{\zeta_0}^{\zeta_1}$ is definitely negative. This time, the competition of $\alpha_{\varphi R}$ versus 2ξ usually declares the victory of the former for sufficiently weakly ionized (thus α_O is large), weakly magnetized disks: because now the values at ζ_0 matter, at which $\varrho = 1$, and $\xi = 2/\beta_0$ is tiny for large β_0 . When the fluid-field coupling at the mid-plane becomes stronger, the inequality $\alpha_{\varphi R} < 2\xi$ may no longer hold, leading to the instability of the symmetric modes. The explorations in §5.2 have already witnessed this situation.

6.1.3. Diffusivities and stabilities

The discussions elaborated above can relate to the physical picture of electric currents and diffusivities. The symmetric modes have non-negligible $|\delta j_{R,\varphi}| = |\partial_\zeta b_{\varphi,R}|$ near $\zeta = 0$, which requires sufficient conductivity to develop. However, weakly ionized PPDs do not have sufficient conductivity there, and the highly resistive plasmas at the mid-plane damp and inhibit the growth of symmetric modes. Such damping depends on α_O more than α_A/b^2 , as the former is generally much greater than the latter at $\zeta \sim 0$, which is consistent with the emphases on Ohmic resistivity in the stability analyses stabilities in e.g. Turner et al. (2007) and Ilgner & Nelson (2008).

Anti-symmetric modes, in contrast, bend their field lines at much higher altitudes (e.g., Figure 4), where the diffusivities are sufficient to support the electric currents required. Ambipolar diffusion is of greater importance at this time since α_O decreases drastically

near the disk surfaces. At the same time, the product $|b_R b_\varphi|$ has much greater absolute values in the term $\alpha_{\varphi R} \simeq -(\alpha_A/b^2)b_R b_\varphi$ (note again that α_A/b^2 is primarily independent of fields and that α_H/b is negligible due to the lack of the $|b_R b_\varphi|$ factor). Qualitatively, this is also consistent with the emphasis on ambipolar diffusion in the analyses of disk stabilities in e.g., Bai & Stone (2011).

The semi-quantitative assumptions and approximations on diffusivities involved for the perturbative analyses have been examined in the elaborations in §4 and §5. At lower disk densities and higher ionization fractions (e.g., magnetized transitional PPDs; Wang & Goodman 2017b), the stability analyses could lead to different conclusions, converging to the situations discussed in §3.

6.2. Predictions of observations

The anti-symmetric modes in PPDs could result in the absence of a magnetized wind on one side of the disk (§4.3). Some young stellar objects (YSOs) have been observed to launch asymmetric winds over both disk surfaces, for example, HH 30 (Burrows et al. 1996; Stapelfeldt et al. 1999). Some other observational evidence supports asymmetric winds (see a review in Pascucci et al. 2023). High spectral resolution [O I] 6300 emission line has been used to trace the disk winds (e.g., Rigliaco et al. 2013; Simon et al. 2016; McGinnis et al. 2018; Fang et al. 2018; Banzatti et al. 2019; Fang et al. 2023a). The line profile of [O I] typically consists of two types of components: a high-velocity component (HVC) and a low-velocity component (LVC). While HVCs are produced in extended jets (Lavalley-Fouquet et al. 2000; Bacciotti et al. 2000; Woitas et al. 2002), LVCs most likely trace MHD winds (Fang et al. 2018; Banzatti et al. 2019; Fang et al. 2023a,b). Though the majority (70%) of LVCs are blueshifted, 21% of LVCs are red-shifted by more than $\gtrsim 1 \text{ km s}^{-1}$ (Fang et al. 2023a). These red-shifted LVCs can be explained if the winds are launched mainly over the disk surface facing away from the observer. Future observational studies are also desired to directly reveal the morphologies of disk winds to confirm the existence of the asymmetries.

The “tilted” accretion may be related to the asymmetric feeding of the central protostar, which is potentially related to the recycling of the accreted materials and the formation of asymmetric jets observed on various PPDs (e.g. Lavalley-Fouquet et al. 2000; Noriega-Crespo et al. 2002; Flores-Rivera et al. 2023). Nevertheless, the innermost accretion regions and the formation of jets in PPDs are complicated, and future studies on the jet morphologies of the jets are required to reveal and confirm the connections between asymmetries in jets and accretion

layers. Meanwhile, accretion lifted to the surface layers also reduces the damping of differential rotation and can induce magnetorotational instabilities (MRI). Once MRI develops in the surface layer, the magnetized wind will be suppressed, and the wind launching area shall exhibit a “truncation” subsequently. Recent observations have been conducted with both spatial and spectral resolutions, which figured out the range of radii for PPD outflows and examined different wind launching mechanisms (e.g. Fang et al. 2023b). Similar high-resolution observations are necessary to confirm these theoretical predictions and understand the complex physical processes that shape magnetized wind structures. For instance, observations that identify the wind launching regions with spatial resolution could establish a direct link between tilted accretion, possible surface MRI, and the suppression of wind launching in PPDs. Both theoretical modeling and high-resolution observations are vital for unraveling the interplay between magnetic fields, turbulence, and gravitational instability.

6.3. Future works

This study focuses on examining the vertical modes with axisymmetry in relation to the wind-driven accretion in protoplanetary disks. This approach does not account for the radial dependence of the problem. A possible extension of this work would involve studying the radial modes, which play a crucial role in the radial transport of magnetic fields. Modulated by the non-ideal MHD features, the radial flux transport and the accretion flow are intertwined and can result in the formation and movement of disk substructures such as rings and gaps. Extending the analytic research on PPD controlled by non-ideal MHD effects, another prospective area of investigation involves examining the breaking of

the disk axisymmetry by azimuthal modes. The close relationship between the azimuthal modes and angular momentum transport in protoplanetary disks can lead to complex phenomena like spiral arms, vortices, and disk warps. Through studying these phenomena, we can better understand how angular momentum transporting is related to different perturbation modes and how that impacts the evolution and dispersal of protoplanetary disks.

Existing theories on PPD substructure gaps often attribute their formation to the influence of existing planets. Nevertheless, a natural mechanism that can produce these structures without the influence of readily formed planets would pave its way to a broader and more generic application. Hence, the proposed study of co-evolved radial, azimuthal, and vertical modes could provide crucial insights into the natural formation of PPD substructures and subsequent evolution over time. Additionally, investigating the interactions of radial modes with the vertical structures and instabilities, possible surface MRI, and even gravitational instabilities on PPD substructure formation could also yield valuable insights for future research. Given that substructures in protoplanetary disks are key to understanding the formation and evolution of planetary systems, this line of research is vital in unlocking some of the mysteries surrounding the early stages of planetary formation.

L. Wang and S. Xu acknowledge the computation resources provided by the Kavli Institute of Astronomy and Astrophysics at Peking University. We thank our colleagues for helpful discussions (alphabetical order of the last names): Can Cui, Gregory Herczeg, Xiao Hu, Haifeng Yang, Xinyu Zheng.

REFERENCES

- Bacciotti, F., Mundt, R., Ray, T. P., et al. 2000, *ApJ*, 537, L49
- Bai, X.-N. 2013, *ApJ*, 772, 96
- . 2017, *ApJ*, 845, 75
- Bai, X.-N., & Stone, J. M. 2011, *ApJ*, 736, 144
- . 2013, *ApJ*, 769, 76
- . 2017, *ApJ*, 836, 46
- Bai, X.-N., Ye, J., Goodman, J., & Yuan, F. 2016, *ApJ*, 818, 152
- Balbus, S. A., & Hawley, J. F. 1991, *ApJ*, 376, 214
- . 1998, *Reviews of Modern Physics*, 70, 1
- Banzatti, A., Pascucci, I., Edwards, S., et al. 2019, *ApJ*, 870, 76
- Béthune, W., Lesur, G., & Ferreira, J. 2017, *A&A*, 600, A75
- Burrows, C. J., Stapelfeldt, K. R., Watson, A. M., et al. 1996, *ApJ*, 473, 437
- Chiang, E. I., & Goldreich, P. 1997, *ApJ*, 490, 368
- Fang, M., Pascucci, I., Edwards, S., et al. 2023a, *ApJ*, 945, 112
- . 2018, *ApJ*, 868, 28
- Fang, M., Wang, L., Herczeg, G. J., et al. 2023b, *Nature Astronomy*, 7, 905
- Flores-Rivera, L., Flock, M., Kurtovic, N. T., et al. 2023, *A&A*, 670, A126
- Gressel, O., Turner, N. J., Nelson, R. P., & McNally, C. P. 2015, *ApJ*, 801, 84

- Harrison, R. E., Looney, L. W., Stephens, I. W., et al. 2021, *ApJ*, 908, 141
- Hu, X., Li, Z.-Y., Zhu, Z., & Yang, C.-C. 2022, *MNRAS*, 516, 2006
- Hu, X., Zhu, Z., Okuzumi, S., et al. 2019, *ApJ*, 885, 36
- Ilgner, M., & Nelson, R. P. 2008, *A&A*, 483, 815
- Latter, H. N., Fromang, S., & Gressel, O. 2010, *MNRAS*, 406, 848
- Lavalley-Fouquet, C., Cabrit, S., & Dougados, C. 2000, *A&A*, 356, L41
- Lesur, G., Kunz, M. W., & Fromang, S. 2014, *A&A*, 566, A56
- Leung, P. K. C., & Ogilvie, G. I. 2020, *MNRAS*, 498, 750
- McGinnis, P., Dougados, C., Alencar, S. H. P., Bouvier, J., & Cabrit, S. 2018, *A&A*, 620, A87
- McNally, C. P., & Pessah, M. E. 2015, *ApJ*, 811, 121
- Nemer, A., Goodman, J., & Wang, L. 2020, *ApJ*, 904, L27
- Noriega-Crespo, A., Coter, A., Young, E., & Chen, H. 2002, *ApJ*, 580, 959
- Owen, J. E., Clarke, C. J., & Ercolano, B. 2012, *MNRAS*, 422, 1880
- Pascucci, I., Cabrit, S., Edwards, S., et al. 2023, in *Astronomical Society of the Pacific Conference Series*, Vol. 534, *Protostars and Planets VII*, ed. S. Inutsuka, Y. Aikawa, T. Muto, K. Tomida, & M. Tamura, 567
- Rigliaco, E., Pascucci, I., Gorti, U., Edwards, S., & Hollenbach, D. 2013, *ApJ*, 772, 60
- Riols, A., Lesur, G., & Menard, F. 2020, *A&A*, 639, A95
- Sano, T., & Miyama, S. M. 1999, *ApJ*, 515, 776
- Sarafidou, E., Gressel, O., Picogna, G., & Ercolano, B. 2024, *MNRAS*, 530, 5131
- Simon, J. B., Bai, X.-N., Armitage, P. J., Stone, J. M., & Beckwith, K. 2013a, *ApJ*, 775, 73
- Simon, J. B., Bai, X.-N., Stone, J. M., Armitage, P. J., & Beckwith, K. 2013b, *ApJ*, 764, 66
- Simon, M. N., Pascucci, I., Edwards, S., et al. 2016, *ApJ*, 831, 169
- Stapelfeldt, K. R., Watson, A. M., Krist, J. E., et al. 1999, *ApJ*, 516, L95
- Turner, N. J., Fromang, S., Gammie, C., et al. 2014, *Protostars and Planets VI*, 411
- Turner, N. J., Sano, T., & Dziourkevitch, N. 2007, *ApJ*, 659, 729
- Vlemmings, W. H. T., Lankhaar, B., Cazzoletti, P., et al. 2019, *A&A*, 624, L7
- Wang, L., Bai, X.-N., & Goodman, J. 2019, *ApJ*, 874, 90
- Wang, L., & Goodman, J. 2017a, *ApJ*, 847, 11
- . 2017b, *ApJ*, 835, 59
- Wardle, M. 2007, *Ap&SS*, 311, 35
- Wardle, M., & Königl, A. 1993, *ApJ*, 410, 218
- Watson, A. M., & Stapelfeldt, K. R. 2004, *ApJ*, 602, 860
- Woitas, J., Ray, T. P., Bacciotti, F., Davis, C. J., & Eislöffel, J. 2002, *ApJ*, 580, 336
- Xu, R., & Bai, X.-N. 2016, *ApJ*, 819, 68

APPENDIX

A. EXTRA TERMS IN THE STEADY-STATE SOLUTION

The general guideline in simplifying the equations for the local wind-driven accretion model is to ignore the terms with R on their denominators or with derivatives of R . In §2.1.2 the inclusion of $\partial_R(v_\varphi B_R)$ (as part of the $\partial_R E_z$ term) has been explained, and this appendix section discusses two other terms with μ_k on the prospectively important denominators.

One of them is associated with J_z , which can be expressed as the derivatives of magnetic fields,

$$\frac{4\pi J_z}{c} = \frac{\partial_R(RB_\varphi) - \partial_\varphi B_R}{R} = \frac{B_\varphi}{R} + \partial_R B_\varphi. \quad (\text{A1})$$

Note that $\partial_\varphi = 0$ strictly holds due to the axisymmetry. While it is unable to examine whether $\partial_R B_\varphi$ plays an essential role with radially local models, the rest (B_φ/R) could still make the terms involving $J_z B_\varphi$ important with sufficiently large $|B_\varphi|$. In the dimensionless form, this product reads $j_z b_\varphi \simeq b_\varphi^2/\mu_k$. As one can observe from the numerical and semi-analytic results in §4.1 and §5, $|b_\varphi|$ could reach $\sim 10^0 - 10^1$, making the $j_z b_\varphi$ term important with $\mu_k \sim 30$ (eq. 4) or even smaller at larger disk radii. Therefore, although $j_z \sim 0$ in eq. (6) essentially holds in most cases, we still include the j_z term when the steady-state solutions are compared to the simulation results in §4.1.

The other term is related to the gravitational force. At $z = 0$, a local model assuming negligible radial pressure gradient has $\partial_R \Phi = v_k^2/R$, where v_k is the Keplerian velocity. In the derivation of the radial momentum equation in eq. (5), this equality is assumed to be true at all altitudes. However, one can prove that $|\partial_R \Phi - v_k^2/R|$ may be no longer negligible at sufficiently high z . This leads to an extra term g_R in the radial momentum equation (eq. 5), using $z/R = \zeta/\mu_k$, and $\partial_z \rightarrow (\mu_k/R)\partial_\zeta$,

$$g_R \equiv -\frac{R(\partial_R \Phi - v_k^2/R)}{\mu_k c_s^2} = \frac{v_k^2}{\mu_k c_s^2} \left[1 - \left(1 + \frac{z^2}{R^2} \right)^{-3/2} \right] = \mu_k \left[1 - \left(1 + \frac{\zeta^2}{\mu_k^2} \right)^{-3/2} \right]. \quad (\text{A2})$$

This approach of approximating radial gravity force is the same as the vertically global shearing box methods elaborated in McNally & Pessah (2015). When we consider the disk surface, $\zeta \sim 3 - 4$, and the g_R could also reach the order of unity. Similar to the terms related to j_z , the g_R is also included to reach better agreements with numerical simulation results. One may notice that a similar correction can also be applied to the vertical momentum equation, yet the other terms dwarf the value of the resulting correction.

B. ELECTRIC CURRENT EQUATIONS FOR STEADY-STATE SOLUTIONS

Assuming $\mu_z \rightarrow 0$, eqs. (5) yield the dimensionless velocity components $\mu_{R,\varphi}$,

$$\mu_\varphi = \frac{j_z b_\phi - j_\varphi}{\beta_0 \varrho} - \frac{g_R}{2}, \quad \mu_R = \frac{4(j_z b_R - j_R)}{\beta_0 \varrho}. \quad (\text{B3})$$

Combining these $\mu_{R,\varphi}$ expressions with eqs. (6) and (7), one gets the equations which shall be solved for $j_{R,\varphi}$,

$$\begin{bmatrix} \alpha_{RR} & \alpha_{R\varphi} + 1/(\beta_0 \varrho) \\ \alpha_{\varphi R} - 4/(\beta_0 \varrho) & \alpha_{\varphi\varphi} \end{bmatrix} \begin{bmatrix} j_R \\ j_\varphi \end{bmatrix} = \begin{bmatrix} \tilde{\varepsilon}_R - g_R/2 + j_z b_\varphi/(\beta_0 \varrho) \\ -4j_z b_R/(\beta_0 \varrho) \end{bmatrix}, \quad (\text{B4})$$

where $\tilde{\varepsilon}_R \equiv \varepsilon_R + \mu_k$ is the dimensionless electric field in the Keplerian rotating frame.

C. MATCHING THE IDEAL MHD WIND SOLUTIONS

Bai et al. (2016) introduced a method of constructing magnetized isothermal wind models above disk surfaces, which is briefly summarized here. This method is based on the conserved quantities along the magnetic field lines, including the Bernoulli parameter H (following from the energy conservation), the mass-field flux ratio k (following from the continuity equation; not to be confused with dimensionless wavenumbers in §3), and the field line angular velocity parameter ω , reading,

$$H = \frac{B_p^2}{2k^2 x^2} + \frac{\omega^2 R^2}{2} \left[\left(\frac{R_A^2/R^2 - 1}{x - 1} \right)^2 - 1 \right] + h - \frac{GM_*}{(R^2 + z^2)^{1/2}}; \quad k \equiv \frac{4\pi \rho v_p}{B_p}, \quad \omega = \Omega - \frac{k B_\varphi}{4\pi \rho R}. \quad (\text{C5})$$

Here M_* is the stellar mass, $x \equiv 4\pi\rho/k^2$ is the density parameter, the subscripts “p” in v_p and B_p indicate the poloidal components of velocities and magnetic fields, R and z are the cylindrical coordinates of the spatial point on the current field line, and R_A marks the radius of the Alfvénic point on the same field line. The thermodynamics of gas elements are involved by the specific enthalpy,

$$h = \int \frac{dp}{\rho} = \begin{cases} c_s^2 \ln\left(\frac{\rho}{\rho_0}\right), & \gamma = 1 \text{ (Isothermal)} ; \\ c_{s0}^2 \left(\frac{\gamma}{\gamma-1}\right) \left(\frac{\rho}{\rho_0}\right)^{\gamma-1}, & \gamma > 1, \end{cases} \quad (\text{C6})$$

where ρ_0 is the wind-base mass density (and the subscript “0” in general marks the quantities at the wind base in this appendix. In our numerical experiments, we found that the MHD profiles yielded by prescribing $\gamma = 7/5$ fit the results in axisymmetric global simulations better than other choices (note that this γ index only applies to the wind, and the disk below the wind base is still vertically isothermal). Since the heating processes largely stop after wind gases finish acceleration and join the wind, this choice also stands closer to a MHD dominated wind whose major component is molecular due to self-shielding and cross-shielding effects of photodissociation (e.g. Wang et al. 2019). The poloidal field B_p in the wind is prescribed as,

$$B_p = B_{p0} \frac{1+q}{(R/R_0) + q(R/R_0)^2}, \quad (\text{C7})$$

in which the parameter q controls the poloidal fields’ transition from parallel to diverging. In practice, we find that $q = 1$ can yield accretion and wind solutions that match the simulation results best. The vertical coordinate z is related to R along the designated field line by a straight-line geometry, $z = z_0 + (R - R_0) \tan \theta$. We adopt $\theta = \tan^{-1}(b_z/b_R)$ at the wind base to guarantee the continuity of magnetic fields. The configuration of poloidal fields in the wind can be calculated accordingly. Physically plausible solutions are obtained by,

$$H = E, \quad \frac{\partial H}{\partial x} = 0, \quad \frac{\partial H}{\partial R} = 0. \quad (\text{C8})$$

In order to construct consistent wind-driven accretion models, the accretion solution described in §2.1 has to be connected to the solution described by eq. (C5) at the wind base, by matching key physical quantities. We first convert eqs. (C5), (C7) into the dimensionless form,

$$\begin{aligned} \mathcal{H} &\equiv \frac{H}{c_s^2} = \left(\frac{b_{p0}^2}{2\tilde{k}^2 x^2}\right) \left(\frac{1+q}{\tilde{R}^2 + q\tilde{R}^2}\right) + \frac{\tilde{\omega}^2 \tilde{R}^2}{2} \left[\left(\frac{\tilde{R}_A^2/\tilde{R}^2 - 1}{x-1}\right)^2 - 1 \right] + \left(\frac{\gamma}{\gamma-1}\right) \left(\frac{x}{x_{\text{wb}}}\right)^{\gamma-1} - \frac{\mu_k^2}{\tilde{r}(R)} ; \\ b_{p0} &\equiv \frac{B_{p0}}{B_{z0}}, \quad \tilde{R} \equiv \frac{R}{R_0}, \quad \tilde{R}_A \equiv \frac{R_A}{R_0} ; \quad x_{\text{wb}} = \left[\left(\frac{2}{\beta_0 \varrho}\right) \tilde{k}\right]_{\text{wb}}^{-1}, \quad \tilde{\omega} \equiv \frac{\omega R_0}{c_s} = \left[(\mu_\varphi + \mu_k) - \left(\frac{2}{\beta_0 \varrho}\right) \tilde{k} b_\phi \right]_{\text{wb}}, \end{aligned} \quad (\text{C9})$$

where the subscript “wb” indicate the wind-base values. The dimensionless $\tilde{k} \equiv kc_s/B_{z0}$ can be obtained by solving the following equation deduced from other conservation quantities,

$$\left(\frac{2b_{\varphi,\text{wb}}\tilde{R}_A^2}{\beta_0 \varrho_{\text{wb}}}\right) \tilde{k}^2 - (\mu_k + \mu_{\varphi,\text{wb}})(\tilde{R}_A^2 - 1)\tilde{k} - b_{\varphi,\text{wb}} = 0. \quad (\text{C10})$$

Each value of \tilde{k} indicates a mass load condition of the wind, which corresponds to a plausible \tilde{R}_A value that allows the wind solution to get through the slow and fast magneto-sonic points smoothly.

We define the wind base at $\mu_R = 0$, separating the accreting and wind-launching regions. The following procedures are taken to obtain a set of solutions with matched wind and accretion profiles:

1. Select a ε_{R0} (the radial component of the mid-plane dimensionless electric field; see §2.1.2) and integrate the steady-state solution to the wind base;
2. Calculate the values of b_{p0} , $\tilde{\omega}$, and \mathcal{H}_{wb} at the wind base;
3. Choose an \tilde{R}_A value and solve for a physically plausible wind solution by solving the algebraic equations $\partial\mathcal{H}/\partial x = \partial\mathcal{H}/\partial\tilde{R} = 0$ for the regularity conditions at both slow and fast magnetosonic points (note that the value of \tilde{k} is obtained by solving eq. C10);

4. Adjust ε_{R0} and conduct Steps 1 through 3 iteratively, so that the \mathcal{H} value in Step 3 equals to the \mathcal{H}_{wb} in Step 2.

We have noticed that matching a wind solution to a radially local accretion solution inevitably leads to the inconsistency of mass conservation, either at the matching point (e.g., this work; Bai et al. 2016) or at the equatorial plane (e.g. Wardle & Königl 1993). However, such inconsistency does not undermine the validity of the background MHD profiles, on which subsequent studies (e.g., the perturbations) are carried out.

D. BOUNDARY CONDITIONS OF PERTURBATION MODES

Inside the wind, the perturbations should be evaluated along the magnetic field lines, and the perturbed quantities should involve μ_z and ∂_R . The radial derivative operator along a field line in the wind satisfies $\partial_R \rightarrow \tan \theta \partial_z$. Still assuming axisymmetry ($\partial_\varphi \rightarrow 0$), the perturbed induction equations read,

$$\nu \delta b_\varphi = -\partial_z \delta \varepsilon_R + \tan \theta \partial_z \varepsilon_z, \quad \nu \delta b_R = \partial_\zeta \delta \varepsilon_\varphi. \quad (\text{D11})$$

As this work aims at the radially local modes that intentionally excludes radial transport of magnetic fluxes, the perturbation $\delta \varepsilon_\varphi$ should vanish, which directly leads to $\delta b_R = 0$. Meanwhile, the perturbed toroidal electric field in the fluid frame $\delta \varepsilon'_\varphi$ should vanish under high conductivity, and the relation $\delta \varepsilon'_\varphi = \delta \varepsilon_\varphi + b_R \delta \mu_z + \mu_z \delta b_R - b_z \delta \mu_R - \mu_R \delta b_z$ also leads to $\delta b_R = 0$ by assuming that the perturbations follow the field line ($\delta b_z = \tan \theta \delta b_R$). This constraint indeed naturally guarantees the solenoidal condition of the perturbed fields, which reads $\nabla \cdot \delta \mathbf{B} = \delta B_R/R + \partial_R \delta B_R + \partial_z \delta B_z = 0$.

With $\delta b_R = 0$ in mind, the perturbation equations inside the wind then read $C_1 \partial_\zeta \delta \vec{b} = C_0 \delta \vec{b}$, in which $\delta \vec{b} \equiv [\delta b_\varphi, \delta \mu_R, \delta \mu_\phi]^T$ and,

$$C_1 \equiv 2 \tan \theta \times \begin{bmatrix} \mu_R & b_\varphi & -b_R \\ 2b_\varphi/(\beta_0 \varrho) & \mu_R & 0 \\ -2b_\varphi/(\beta_0 \varrho) & 0 & 2\mu_R \end{bmatrix}, \quad C_0 \equiv \nu I + 2 \tan \theta \times \begin{bmatrix} \partial_\zeta \mu_R & \partial_\zeta b_\varphi & -\partial_\zeta b_R \\ \partial_\zeta b_\varphi/(\beta_0 \varrho) & \partial_\zeta \mu_R & -\cot \theta \\ 0 & (\cot \theta)/4 + \partial_\zeta \mu_\phi & 0 \end{bmatrix}. \quad (\text{D12})$$

At the wind base ζ_{wb} , a perturbation mode is connected to the wind perturbations (eqs. D12) by adopting the $\delta \mu_R$ and $\delta \mu_\phi$ obtained from eqs. (10), and the integration continues to an stopping altitude $\zeta_1 \geq \zeta_{\text{wb}}$. Ideally, one could set $\zeta_1 \rightarrow \infty$ and aim at vanishing $\{\delta b_R, \delta b_\varphi\}$ by adjusting the eigenvalue ν and the free parameter $\delta j_{\varphi 0}$ (symmetric) or $\delta b_{\varphi 0}$ (anti-symmetric). However, the integration to infinity is difficult and unnecessary, especially when one considers the difficulties of perturbation modes passing through the critical points (including the poloidal Alfvénic point, and the slow and fast magnetosonic points). In a variety of numerical experiments, we choose different finite ζ_1 values, to verify that ν changes by no more than $\sim 10\%$ as long as $\zeta_1 \geq \zeta_{\text{wb}}$, even if ζ_1 is located at the poloidal Alfvénic point (Appendix C) that is typically $\gtrsim 10$ scale heights above ζ_{wb} . This can also be qualitatively explained if one inspects eq. (D12) for an leading-order asymptotic approximation regarding ϱ^{-1} and δb_φ ,

$$b_\varphi \partial_\zeta \delta b_\varphi \simeq \delta b_\varphi \partial_\zeta b_\varphi \Rightarrow \delta b_\varphi \lesssim b_\varphi, \quad (\text{D13})$$

which holds when $\varrho \ll 1$, a quite typical condition within the wind region. Since $B_\varphi \propto R^{-1}$ inside the magneto-thermal wind (e.g. Bai et al. 2016), δb_φ decays rather slowly at relatively large altitudes. Therefore, the altitude of setting $\delta b_\varphi = 0$ does *not* affect the eigenmodes significantly. For simplicity and clarity, we fix $\zeta_1 = \zeta_{\text{wb}}$ and adjust the free parameters so that $\delta b_R|_{\zeta=\zeta_1} = \delta b_\varphi|_{\zeta=\zeta_1} = 0$.